PHYSICAL REVIEW B **93**, 041104(R) (2016)

Ferroelectric instability and topological crystalline insulating nature in PbPo

Chang-Jong Kang* and B. I. Min†

Department of Physics, PCTP, Pohang University of Science and Technology, Pohang 37673, Korea

(Received 22 November 2015; published 13 January 2016)

We have investigated the lattice instability and the topological property of the electronic structure in PbPo in comparison with other IV-VI semiconductors, SnTe and PbTe. In the conventional exchange-correlation schemes of the density functional theory, the fcc structure of PbPo tends to be unstable in the presence of spin-orbit coupling (SOC) under [111] distortion so as to have a ferroelectric instability. This feature is revealed in the calculated phonon dispersion of PbPo by the phonon softening instability at $\mathbf{k} = \Gamma$. But, in the modified Becke-Johnson (mBJ) potential scheme, we have shown that the tendency for SOC-driven ferroelectric instability is suppressed, and the fcc structure becomes stabilized. We have demonstrated that PbPo is a semiconductor having a band inversion at $\mathbf{k} = L$, which leads to a topological crystalline insulator (TCI) phase of PbPo, and the TCI and the ferroelectric states coexist for moderate [111] distortions.

DOI: 10.1103/PhysRevB.93.041104

A topological crystalline insulator (TCI), which is a new class of topological materials beyond Z_2 topological insulators [1], was proposed recently [2], and has attracted a great deal of recent attention [3–8]. Narrow band gap IV-VI semiconductors, such as SnTe [3,4] and $Pb_{1-x}Sn_xTe/Se$ [4–8], were reported to be TCIs. A key characteristic of TCIs is that metallic surface states are protected by crystal symmetry rather than time-reversal symmetry. Recently, Liu *et al.* [9] proposed a topological transistor device in thin films of TCIs, which has two pairs of spin-filtered edge states with an electric field tunable gap. Therefore, TCIs are very promising for future device applications.

In this Rapid Communication, we propose that PbPo, which also belongs to a IV-VI semiconductor, has the possibility of being a TCI. PbPo is formed from the alpha decay of simple-cubic Po, and it crystallizes in a NaCl-type fcc with a lattice constant of $a = 6.590$ Å [see Fig. 1(a)] [10,11]. Due to its toxic nature, there exist only a few experimental reports so far [11], and most of the physical properties of PbPo were predicted theoretically [12–16]. Based on empirical evidence, Dalven [12,17] once argued that PbPo would have a possible band inversion at L ($L^+_{4,5}$, L^-_6, and L^+_6 in ascending energy order) and have a band gap of 0.1 eV at 77 K. On the other hand, based on density functional theory (DFT), Rabii *et al.* [14,15] reported that PbPo is a semimetal with L^-_6, $L^+_{4,5}$, and L^+_6 in ascending energy order. However, the calculations by Rabii *et al.* were done by using the conventional DFT, and so more advanced band methods are needed to check the electronic structure of PbPo.

We have studied the electronic structures and phonon properties of IV-VI semiconductors, such as SnTe, PbTe, and PbPo, based on the state-of-the-art DFT. We have found that conventional DFT schemes tend to underestimate the band gaps of IV-VI semiconductors, while advanced band methods using the modified Becke-Johnson (mBJ) exchange potential and G_0W_0 methods produce correct band gaps that are comparable to the experimental values. Besides, the mBJ method also describes the equilibrium lattice constants well. Furthermore, the calculated phonon dispersion for fcc PbPo within conventional DFT schemes reveals phonon softening instability in the presence of spin-orbit coupling (SOC), which is related to the [111] lattice and ferroelectric instabilities observed in other IV-VI semiconductors. But, in the mBJ scheme, the tendency for SOC-driven ferroelectric instability is found to be suppressed, and the fcc structure becomes stabilized. We have shown that fcc PbPo is a semiconductor with a band inversion at L, which leads to PbPo being a TCI.

We have employed the all-electron full-potential linearized augmented plane-wave (FLAPW) band method implemented in WIEN2K [18]. We used $36 \times 36 \times 36$ **k**-point mesh in the full Brillouin zone. The muffin-tin radii R_{MT} were set to 2.50 a.u. for Pb and Po, and the product of R_{MT} and the maximum reciprocal lattice vector K_{max} was chosen as $R_{MT} \cdot K_{max} = 7$ [19]. We used the maximum L value of 10 for the orbital basis inside the muffin-tin spheres and the largest reciprocal lattice vector G_{max} of 12 in the charge Fourier expansion. The SOC is treated in the second variational way. To check the functional dependency, we have used the local-density approximation (LDA), the Perdew-Burke-Ernzerhof (PBE) [20], which is a standard generalized-gradient approximation (GGA), and its modification designed specifically for solids (PBEsol) [21]. We have also used the mBJ method [22,23] and the G_0W_0 method [24] implemented in VASP [25] to get an accurate band gap. For the G_0W_0 calculation, we have used 100 unoccupied states with an $8 \times 8 \times 8$ **k**-point grid centered at the Γ point. An energy cutoff of 400 eV was used for the number of plane-wave bases.

For phonon calculations, we have employed the VASP and the PHONOPY codes [26]. The force constants and the dynamical matrix are obtained from the Hellmann-Feynman forces calculated with small individual displacements of nonequivalent atoms in a $(4 \times 4 \times 4)$ supercell of a primitive unit cell. A $5 \times 5 \times 5$ **k**-point mesh was used for the force calculation.

To explore the surface states, we have employed the slab calculations, and we have used the maximally localized Wannier function (MLWF) [27,28] implemented in the WANNIER90 code [29]. The construction of MLWF is performed on $27 \times 27 \times 27$ **k**-point meshes with the formerly converged self-consistent charge and potential obtained by WIEN2K. We considered a 300-layer slab in the calculations.

*rkdc1234@postech.ac.kr
†bimin@postech.ac.kr

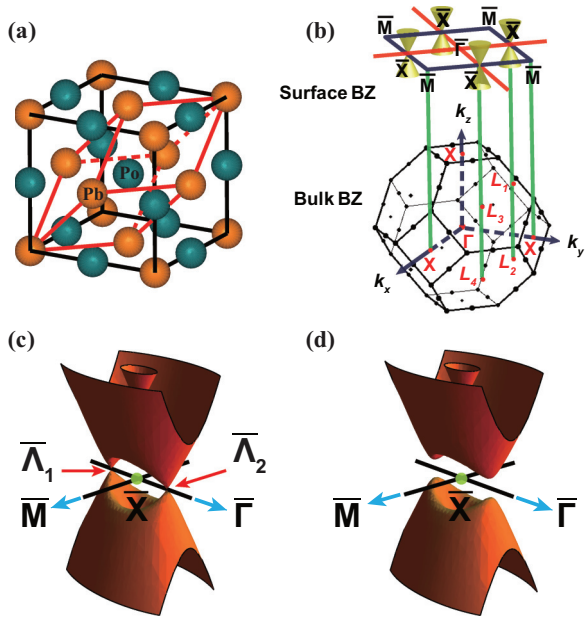

FIG. 1. (a) NaCl-type crystal structure of PbPo. Black and red lines represent conventional and primitive unit cells, respectively. (b) Bulk and surface Brillouin zones (BZs) for a primitive unit cell of PbPo. A band inversion at L of bulk BZ leads to double Dirac cones at $\bar{X}$. (c) Massless double Dirac cones near $\bar{X}$. The hybridization between double Dirac cones is not allowed along the $\bar{\Gamma}$-$\bar{X}$ direction due to crystal mirror symmetry, and so two Dirac points emerge at $\bar{\Lambda}_1$ and $\bar{\Lambda}_2$. (d) Massive double Dirac cones near $\bar{X}$ in the presence of [111] distortion. Since [111] distortion breaks (110) crystal mirror symmetry, the double Dirac cones become massive.

Table I presents the equilibrium lattice constants and band gaps of SnTe, PbTe, and PbPo, which are obtained within the DFT level. For comparison, the experimental data are also presented. The general tendency is clearly shown in that the LDA (PBE) functional yields an equilibrium lattice constant that is shorter (longer) than the experimental one. The PBEsol functional is devised to improve the equilibrium properties of solids [21] and gives equilibrium lattice constants that are better than the LDA and PBE functionals. However, the band gaps are underestimated in the PBEsol functional. The mBJ with the SOC (mBJ+SOC) scheme is seen to describe both equilibrium lattice constants and band gaps more properly than other schemes. It is noteworthy that the band gap opens in PbPo only by the mBJ. In fact, the mBJ method was thoroughly tested for many semiconductors and insulators, to obtain band gaps close to the experimental ones [22]. We have checked that the G_0W_0 method also produces the gap feature as shown in Fig. 3(d), which confirms the mBJ result. Thus, in view of a much reduced computational time, the mBJ is indeed an efficient method to get a reasonable band gap.

TABLE I. Calculated equilibrium cubic lattice constants (Å) and band gaps (eV_) for IV-VI semiconductors, SnTe, PbTe, and PbPo, in comparison with experimental data. For PbPo, only the mBJ+SOC yields a band gap, and there is no experimental datum available.

	SnTe		PbTe		PbPo	
With SOC	a_{eq}	E_{gap}	a_{eq}	E_{gap}	a_{eq}	E_{gap}
LDA	6.242	0.277	6.370	0.145	6.515	(−)
PBE	6.402	0.218	6.556	0.200	6.718	(−)
PBEsol	6.286	0.271	6.426	0.125	6.576	(−)
mBJ	6.282	0.178	6.424	0.207	6.602	0.093
Expt.	6.318[a]	0.2[b]	6.443[c]	0.18[d]	6.590[e]	(·)

[a]Reference [30].
[b]Reference [31].
[c]Reference [32].
[d]Reference [33].
[e]Reference [11].

Figure 2(a) shows phonon dispersions of PbPo within the PBEsol functional without and with the SOC schemes. The SOC makes the optical phonon modes more softened to have imaginary phonon frequencies at Γ. The normal mode having an imaginary phonon frequency is shown in the inset of Fig. 2(b), which corresponds to [111] distortion. In fact, this distortion is related to ferroelectric instability. The total energy versus [111] distortion is presented in Fig. 2(b). The PBEsol without SOC has minimum energy at zero distortion and gives higher energy with increasing [111] distortion. It means that the NaCl-type fcc structure is stable, which is consistent with the phonon dispersion in Fig. 2(a). In contrast, the PBEsol with the SOC (PBEsol+SOC) scheme yields a fcc structure that is unstable for [111] distortion. The [111]

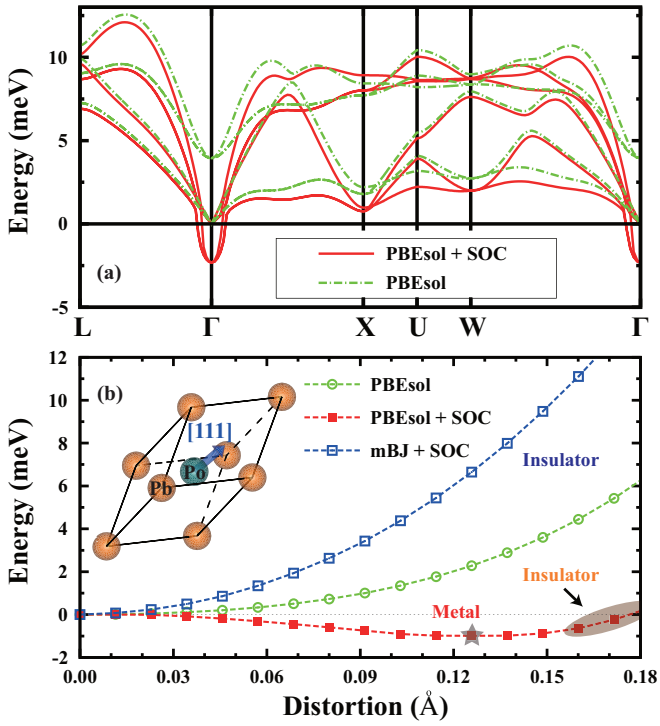

FIG. 2. (a) Phonon dispersions of PbPo in the PBEsol without and with the SOC schemes. The SOC makes the Γ-point optical phonon modes have imaginary phonon frequencies. The corresponding normal modes are shown in the inset of (b), which corresponds to [111] distortion. (b) Total energy vs [111] distortion. The PBEsol+SOC scheme yields the instability of the NaCl-type structure under [111] distortion, with minimum energy at finite distortion (gray star), and a metal to insulator transition for distortions of larger than 0.16 Å. The PBEsol (without the SOC) and mBJ+SOC schemes, however, yield a stable NaCl-type structure against [111] distortion.

distortion up to a magnitude of 0.16 Å gives a metallic phase, but the insulating phase emerges beyond it, which corresponds to a Peierls-type distortion.

The SOC-induced lattice instability behavior in PbPo is quite opposite to the case in simple-cubic Po [34–36], where the SOC instead stabilizes the simple-cubic structure against [111] Peierls distortion. The reason for the opposite behavior would be related to the different bonding nature between the two, namely, simple-cubic Po has a more covalent-bonding nature while PbPo has a more ionic-bonding nature. Note that the Born effective charges of Pb and Po without the SOC (with the SOC) scheme give +6.20 (+8.19) and −6.20 (−8.19), respectively, which indicates that the SOC increases the Born effective charges of both Pb and Po atoms and triggers ferroelectric instability.

According to Fig. 2(b), however, the NaCl-type structure is stable against [111] distortion in the mBJ+SOC scheme. As shown in Table I, the mBJ scheme describes the physical properties of PbPo better than other schemes [22,23]. Hence, it is more likely that the NaCl-type fcc structure of PbPo is stable, which is indeed consistent with experiments [11]. We have also examined the phonon dispersions of fcc PbPo at elevated temperatures within the PBEsol+SOC scheme [37], and found that there is no imaginary phonon softening at $T = 300$ K (see the Supplemental Material [38]). This indicates that, even in the PBEsol+SOC scheme, the NaCl-type fcc structure of PbPo would be stable at high temperatures.

Figure 3 shows the electronic band structures of PbPo in several schemes. Band structures in the PBEsol and mBJ schemes with SOC are shown in Fig. 3(a). The PBEsol+SOC scheme yields that the valence band along the Γ-K direction and the conduction band along the Γ-L direction cross the Fermi level (E_F), resulting in a semimetallic phase. However, the mBJ+SOC scheme yields an insulating phase with a band gap of 93 meV.

The band structure in the PBEsol scheme (without SOC) yields an insulating phase with a band gap of 0.35 eV, as shown in Fig. 3(b). The valence and conduction bands are mainly composed of Po p and Pb p, respectively, and there is no band inversion. On the other hand, the band structure in the PBEsol+SOC scheme in Fig. 3(c) shows the band/parity inversion at L between the L_6^+ and L_6^- bands. However, as shown in Fig. 3(a), there is a slight overlap between the conduction and valence bands, which breaks the charge gap protection. The band symmetries are L_6^-, $L_{4,5}^+$, and L_6^+ in ascending energy order, which is consistent with Rabii's argument [14,15]. The band structure in the mBJ+SOC in Fig. 3(d) shows the band/parity inversion at L between L_6^+ and L_6^- bands with a finite band gap. The band symmetries in this case are $L_{4,5}^+$, L_6^-, and L_6^+ in ascending energy order, which is consistent with Dalven's argument [12]. The green dots in Fig. 3(d) represent the G_0W_0 quasiparticle energies. It is seen that the G_0W_0 scheme gives a larger direct band gap at L than the mBJ+SOC scheme. The gap feature at L in the G_0W_0 scheme suggests that the mBJ+SOC scheme describes the electronic structure of PbPo better than the PBEsol+SOC scheme.

Figure 4 shows the (001) surface band structures of PbPo in the mBJ scheme. The mBJ without SOC in Fig. 4(a) yields

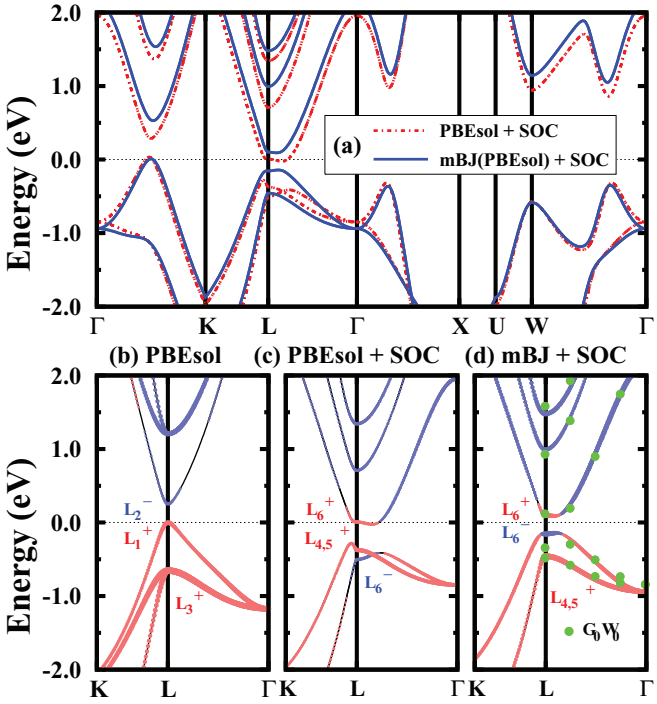

FIG. 3. (a) Band structures in the PBEsol and mBJ schemes with the SOC. (b), (c), and (d) are band structures of PbPo along K-L-Γ in PBEsol, PBEsol+SOC, and mBJ+SOC, respectively. Red and blue dots represent Po p and Pb p characters, respectively. Green dots in (d) represent the G_0W_0 quasiparticle energies.

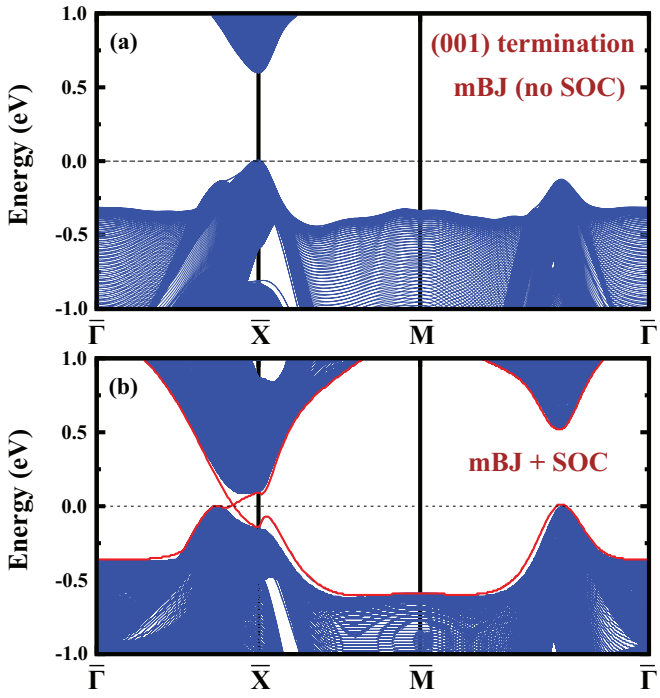

FIG. 4. Bulk and surface band structures of PbPo with (001) termination. (a) Band structure in the mBJ without SOC. Since no band/parity inversion occurs without SOC, no surface states emerge. (b) Band structure in the mBJ+SOC scheme. Since band/parity inversion occurs at L, the topologically protected surface states appear near E_F. The surface states in (b) are visualized in Fig. 1(c) in the three-dimensional (3D) version.

no band/parity inversion, and so there is no topologically protected in-gap surface states. Figure 4(b) presents the band structure in the mBJ+SOC scheme. Since the band/parity inversion occurs at L in this case, the topologically protected in-gap surface states emerge near E_F. These surface states produce double Dirac cones near $\bar{X}$, as discussed in Fig. 1(c), and so PbPo is expected to be a TCI.

It is noteworthy that the lattice and ferroelectric instabilities are driven by SOC, but the induced electric polarization around the atoms having considerable ionicity in turn tends to suppress lattice instability. Namely, competition occurs between the SOC-driven ferroelectric instability and the induced electric polarization. In the case of PbPo, the induced electric polarization wins over lattice instability, and so the fcc structure is stable, as shown in Fig. 2(b). We have also found that the band inversion in the semiconducting state persists under a moderate amount of [111] distortion, suggesting that the topological nature is robust under [111] distortion. In the presence of [111] distortion, one pair of Dirac cones in Fig. 1(b) becomes massive due to broken (110) crystal mirror symmetry [Fig. 1(d)], while the others remain massless because they still possess $(1\bar{1}0)$ crystal mirror symmetry [Fig. 1(c)]. Therefore, the ferroelectric and the TCI phases could coexist in the semiconducting phase of PbPo. This coexistence of two exotic phases is promising for future device applications as well as for academic perspectives.

We have investigated the electronic structures and phonon properties of PbPo and other IV-VI semiconductors, SnTe and PbTe, based on the state-of-the-art DFT. We have found that the conventional DFT scheme, such as the LDA, PBE, and PBEsol, tend to underestimate the band gaps of IV-VI semiconductors, whereas both the mBJ and G_0W_0 schemes give correct band gaps that are comparable to experimental values. The equilibrium lattice constants are also described better by the mBJ method. Furthermore, in the mBJ scheme, the tendency for the SOC-driven ferroelectric instability is suppressed so as to retain the fcc structure, and PbPo becomes a semiconductor with a band gap of 93 meV. In the semiconducting phase, the band inversion occurs at L, which leads to PbPo being a TCI. We hope that these findings could spur further experiments on IV-VI semiconducting materials including PbPo.

This work was supported by the NRF of Korea (Grant No.2015R1A2A1A15053564), the POSTECH BK21Plus Physics Division, and the KISTI supercomputing center (No. KSC-2015-C3-007).

[1] M. Z. Hassan and C. L. Kane, Rev. Mod. Phys. **82**, 3045 (2010).
[2] L. Fu, Phys. Rev. Lett. **106**, 106802 (2011).
[3] Y. Tanaka, Z. Ren, T. Sato, K. Nakayama, S. Souma, T. Takahashi, K. Segawa, and Y. Ando, Nat. Phys. **8**, 800 (2012).
[4] J. Liu, W. Duan, and L. Fu, Phys. Rev. B **88**, 241303(R) (2013).
[5] S.-Y. Xu, C. Liu, N. Alidoust, M. Neupane, D. Qian, I. Belopolski, J. D. Denlinger, Y. J. Wang, H. Lin, L. A. wray, G. Landolt, B. Slomski, J. H. Dil, A. Marcinkova, E. Morosan, Q. Gibson, R. Sankar, F. C. Chou, R. J. Cava, A. Bansil, and M. Z. Hasan, Nat. Commun. **3**, 1192 (2012).
[6] P. Dziawa, B. J. Kowaiski, K. Dybko, R. Buczko, A. Szczerbakow, M. Szot, E. Łusakowska, T. Balasubramanian, B. M. Wojek, M. H. Berntsen, O. Tjernberg, and T. Story, Nat. Mater. **11**, 1023 (2012).
[7] Y. Okada, M. Serbyn, H. Lin, D. Walkup, W. Zhou, C. Dhital, M. Neupane, S. Xu, Y. J. Wang, R. Sankar, F. Chou, A. Bansil, M. Z. Hasan, S. D. Wilson, L. Fu, and V. Madhavan, Science **341**, 1496 (2013).
[8] T. H. Hsieh, H. Lin, J. Liu, W. Duan, A. Bansil, and L. Fu, Nat. Commun. **3**, 982 (2012).
[9] J. Liu, T. H. Hsieh, P. Wei, W. Duan, J. Moodera, and L. Fu, Nat. Mater. **13**, 178 (2014).
[10] J. M. Goode, J. Chem. Phys. **26**, 1269 (1957).
[11] W. G. Witteman, A. L. Giorgi, and D. T. Vier, J. Phys. Chem. **64**, 434 (1960).
[12] R. Dalven, Phys. Rev. Lett. **28**, 91 (1972).
[13] R. Dalven, J. Phys. C: Solid State Phys. **6**, 671 (1973).
[14] S. Rabii and R. H. Lasseter, Phys. Rev. Lett. **33**, 703 (1974).
[15] S. Rabii, Phys. Rev. B **18**, 1876 (1978).
[16] Y. Bencherif, A. Boukra, A. Zaoui, and M. Ferhat, Physica B **407**, 3520 (2012).
[17] R. Dalven, Phys. Rev. Lett. **24**, 1015 (1970).
[18] P. Blaha, K. Schwarz, G. K. H. Madsen, D. Kavasnicka, and J. Luitz, *Wien2k* (Karlheinz Schwarz, Technische Universitat Wien, Austria, 2001).
[19] We have also check electronic structures with $R_{\mathrm{MT}} \cdot K_{\max} = 9$ and have found no major change compared to $R_{\mathrm{MT}} \cdot K_{\max} = 7$.
[20] J. P. Perdew, K. Burke, and M. Ernzerhof, Phys. Rev. Lett. **77**, 3865 (1996).
[21] J. P. Perdew, A. Ruzsinszky, G. I. Csonka, O. A. Vydrov, G. E. Scuseria, L. A. Constantin, X. Zhou, and K. Burke, Phys. Rev. Lett. **100**, 136406 (2008).
[22] F. Tran and P. Blaha, Phys. Rev. Lett. **102**, 226401 (2009).
[23] D. Koller, F. Tran, and P. Blaha, Phys. Rev. B **85**, 155109 (2012).
[24] M. Shishkin and G. Kresse, Phys. Rev. B **75**, 235102 (2007).
[25] G. Kresse and J. Furthmüller, Phys. Rev. B **54**, 11169 (1996); Comput. Mater. Sci. **6**, 15 (1996).
[26] A. Togo, F. Oba, and I. Tanaka, Phys. Rev. B **78**, 134106 (2008).
[27] N. Marzari and D. Vanderbilt, Phys. Rev. B **56**, 12847 (1997).
[28] I. Souza, N. Marzari, and D. Vanderbilt, Phys. Rev. B **65**, 035109 (2001).
[29] A. A. Mostofi, J. R. Yates, Y.-S. Lee, I. Souza, D. Vanderbilt, and N. Marzari, Comput. Phys. Commun. **178**, 685 (2008).
[30] P. B. Pereira, I. Sergueev, S. Gorsse, J. Dadda, E. Müller, and R. P. Hermann, Phys. Status Solidi B **250**, 1300 (2013).
[31] R. Tsu, W. E. Howard, and L. Esaki, Phys. Rev. **172**, 779 (1968).
[32] A. N. Mariano and K. L. Chopra, Appl. Phys. Lett. **10**, 282 (1967).
[33] J. O. Dimmock, I. Melngailis, and A. J. Strauss, Phy. Rev. Lett. **16**, 1193 (1966).

[34] B. I. Min, J. H. Shim, M. S. Park, K. Kim, S. K. Kwon, and S. J. Youn, Phys. Rev. B **73**, 132102 (2006).

[35] K. Kim, H. C. Choi, and B. I. Min, Phys. Rev. Lett. **102**, 079701 (2009).

[36] C.-J. Kang, K. Kim, and B. I. Min, Phys. Rev. B **86**, 054115 (2012).

[37] P. Souvatzis, O. Eriksson, M. I. Katsnelson, and S. P. Rudin, Phys. Rev. Lett. **100**, 095901 (2008).

[38] See Supplemental Material at http://link.aps.org/supplemental/10.1103/PhysRevB.93.041104 for the temperature-dependent DFT phonon dispersions.